Delamination of Nickel–Cobalt Oxyhydroxides for Electrochemical Energy Storage Applications

Alberto Adan-Mas [1,2], Jacob Olchowka [2,3], Lydie Bourgeois [4], Philippe Legros [5], Patrizia Paradiso 6, Fátima Montemor [1], Liliane Guerlou-Demourgues [2,3]

1) Centro de Química Estrutural-CQE, DEQ, Instituto Superior Técnico, Universidade de Lisboa, 1049-001 Lisboa, Portugal

2) Bordeaux INP, ICMCB UMR 5026, CNRS, University of Bordeaux, 33600 Pessac, France

3) RS2E, Réseau Français sur le Stockage Electrochimique de l'Energie, CNRS 345980039 Amiens Cedex 1, France

4) Groupe de Spectroscopie Moléculaire, Université de Bordeaux, ISM, F-33405Talence, France; Bordeaux INP, ISM, CNRS UMR 5255, F-33405 Talence, France

5) PLACAMAT UMS 3626, CNRS-Université de Bordeaux, F-33608 Pessac Cédex, France

6) IDMEC–Instituto de Engenharia Mecánica, Universidade de Lisboa, 1049-001 Lisboa, Portugal

Abstract

Nickel–cobalt oxyhydroxide has been delaminated by tetrabutylammonium (TBA^+) intercalation in aqueous media. The electrochemical performance of the different materials obtained during delamination has been evaluated, with special emphasis on the effect of the intercalated species and their influence on the behavior of the delaminated material, toward electrochemical energy storage applications. Delamination in TBAOH, reported for the first time for nickel–cobalt oxyhydroxide in aqueous media, is an excellent route to increase the number of electrochemically active sites and to enhance the capacity of nickel–cobalt oxyhydroxide. Results show an increase in capacity from 112 $mA{\cdot}h{\cdot}g^{-1}$ in 1 M LiOH at 1 $A{\cdot}g^{-1}$ for the nondelaminated precursor to 165 $mA{\cdot}h{\cdot}g^{-1}$ after exfoliation and restacking. Thus, carefully designed exfoliation is a promising route to enhance the performance of electrode materials for electrochemical energy storage.

Keywords :

- Nickel−cobalt oxyhydroxide
- Delamination
- Chemical exfoliation
- Energy storage
- Nickel−cobalt oxide
- Tetrabutylammonium intercalation

Introduction

The electrochemical performance of energy storage devices depends on the selection of electrode materials, which are usually optimized to obtain maximum capacity/capacitance, specific power, or cycling stability, depending upon application. Nonetheless, active surface area is always a critical parameter. Related to charge storage, chemical and morphological stability, electrode–electrolyte interaction, and electron and ion transport; a maximized surface area is of extreme importance in the development of novel materials, especially for high-power applications. For that reason, nanostructured materials, in particular two-dimensional layered materials, have become a field of great interest. [1]

Layered double hydroxides (LDHs), also known as anionic clays, have been pinpointed as promising pseudocapacitive materials because of their high redox activity, low cost, and environmental friendliness. LDHs are two-dimensional ionic lamellar materials consisting of positively charged brucite-like layers with an interlayer region containing either solvent molecules or anionic species. [2] However, layered double hydroxide materials present a major limitation: reduced accessibility to the inner surface of the host layers by the electrolyte, which leads to reduced active surface area for energy storage applications. For that reason, many efforts have been made to delaminate such materials. In addition, if the material is successfully delaminated, the positively charged layers can work as building blocks to produce functional materials by integrating them with negatively charged species.

Consequently, many attempts have been done to exfoliate different types of LDHs. [2] The most common procedure consists of the intercalation of molecules/ions in the interlamellar space and the subsequent delamination in an appropriate solvent. Many solvents have been used, such as butanol, [3] acrylates, [4] toluene, [5] or formamide, [6,7] among others.

However, from an environmental and practical perspective, it is of great interest to achieve delamination in water. The first reported aqueous-based delamination was performed by Hibino and Kobayashi [8] for Mg–Al–lactate. The method presents three main advantages compared to delamination in organic solvents, namely, the exclusive use of water, the higher concentration achieved in the delaminated colloidal suspension, and, finally, the fact that the synthesis process does not require heat. Henceforward, other materials have been delaminated in a similar fashion, such as Zn–Al–lactate. [9]

Nickel (hydr)oxide and cobalt (hydr)oxide exfoliations are of special interest for electrochemical energy storage applications. [10−12] On the one hand, nickel-based materials, predominantly NiO and $Ni(OH)_2$, exhibit a well-known electrochemical activity due to faradaic processes but their high resistivity limits their performances. [13] Cobalt-based materials (Co_3O_4 and Co oxyhydroxides) are also promising candidates due to their excellent reversible redox reactions that translate into good cycling stability [13,14] as well as their high conductivity, especially if they contain mixed-valence Co^{3+}/Co^{4+}. [15] However, they present either low-capacity values or short potential ranges and, for that reason, its combination with nickel (hydr)oxides is of great interest. Consequently, nickel–cobalt oxyhydroxides were considered for delamination and electrochemical energy storage electrode applications in this work.

Nickel hydroxide, cobalt hydroxide, and nickel–cobalt hydroxides were successfully delaminated in water by the intercalation of lactates by Lang et al., [16−18] and their electrochemical performance was studied by means of cyclic voltammetry. Another known route is the exfoliation of oxide and oxyhydroxide materials by means of cation intercalation. [19] A common feature of layered oxides is their cation-exchange property, which enables the modification of the interslab space, ultimately leading to exfoliation. As Sasaki and Ma pointed out, [20] there is a well-established route for the exfoliation of layered metal oxides, which consists of first a solid-state calcination synthesis of precursor materials with posterior acidification to produce their hydrated protonic form. Then, these can be modified with positively charged bulky organic ions (TMA^+, TBA^+, etc.) that increase the interlayer distance, decrease the electrostatic interaction between the layers, and enable their delamination. For instance, Tang et al. recently used this approach to exfoliate birnessite manganese dioxide and cobalt oxyhydroxide in order to perform a controlled restacking to obtain homogeneous Mn–Co composites with enhanced electrochemical performance. [21,22] Several materials have been exfoliated in that manner, such as MnO_2, [19] TaO_3 [23] or $HCoO_2$. [24] However, to the best of the author's knowledge, neither delamination of nickel nor mixed nickel–cobalt oxyhydroxide has been proposed for electrochemical energy storage applications.

The different materials obtained during the delamination process of nickel–cobalt oxyhydroxide materials in water, by means of TBA^+ intercalation, are characterized and studied here as potential electrode materials for charge storage in alkaline media. Finally, the influence of different cations in the electrolyte, namely, K^+ and Li^+, is considered during the charge–discharge of the different active materials and its role discussed.

Experimental Section

Exfoliation of Nickel–Cobalt Oxyhydroxide

The process used for the delamination of nickel–cobalt oxyhydroxide nanoslabs in tetrabutylammonium hydroxide is exemplified in Figure 1 and detailed hereinafter. It is worth noting that, in all experimental steps, the metal (oxyhydr)oxide layer remains unchanged and is characterized by MO_6 edge sharing octahedral units. During the delamination, M–O distances could slightly be modified depending on the M^{n+} oxidation state, but changes mainly occur in the interlayer spacing, where ion substitutions occur.

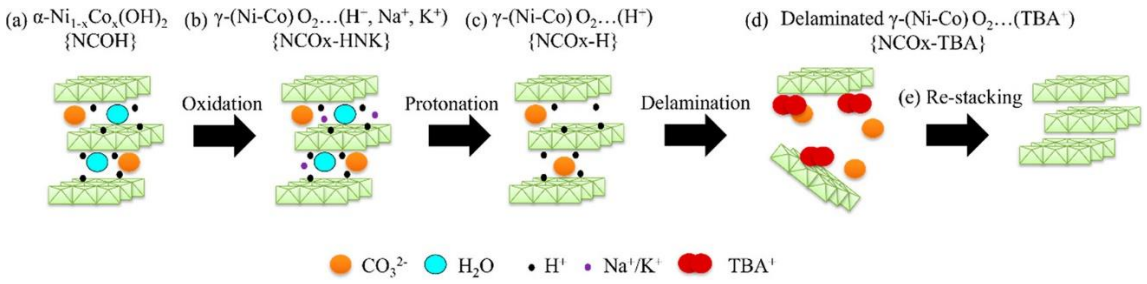

Figure 1. Schematic of the exfoliation process for γ-$Ni_xCo_{1-x}O_2$ nanoslabs that includes (a) α-nickel–cobalt hydroxide, (b) γ-nickel–cobalt oxyhydroxide, (c) protonated γ-nickel–cobalt oxyhydroxide, (d) delaminated γ-nickel–cobalt oxyhydroxide, and (e) restacked γ-nickel–cobalt oxyhydroxide.

Synthesis of α-Nickel–Cobalt Hydroxide

Typically, 5 g of nickel nitrate hexahydrate and 10 g of cobalt nitrate hexahydrate were dissolved in 100 mL of distilled water. 40 mL of 2M NaOH containing 1.5 mL of H_2O_2 was quickly poured in the solution, forming a green-brown precipitate of α-Ni-Co$(OH)_2{\cdot}(CO_3^{2-}, 2NO_3^-)_y$. This solution was aged for 24 h. It was then centrifuged at 4000 rpm for 5 min and washed with H_2O and ethanol 6 times until neutral pH to remove impurities. Approximately 7 g of the α phase, named as NCOH {nickel cobalt hydroxide}, was recovered after the powder was dried at 40 °C for 24 h.

Oxidation Reaction to γ-Nickel–Cobalt Oxyhydroxide

2.6 g of NCOH was suspended in a mixture of 20 mL of 10M NaClO (Prolabo) with 80 mL of 5M KOH and kept under stirring for 24 h. The resulting suspension was centrifuged at 4000 rpm for 5 min. Once the powder was recovered, it was washed 5 times with distilled water and several times with ethanol until neutral pH. 2.2 g of the resulting γ-phase was recovered and named as NCOx-HNK {as in nickel–cobalt oxide intercalated with protons (H), sodium (Na), and potassium (K)}.

Protonation of γ-Nickel–Cobalt Oxyhydroxide

1.8 g of NCOx-HNK was suspended in 150 mL of 10 mM HNO_3 and stirred overnight. The resulting product is a protonated version of the γ phase in which the sodium and potassium ions intercalated in the interslab space of material are exchanged by protons. After washing with distilled water and ethanol several times until neutral pH is reached, 1.39 g of product was recovered and designated as NCOx-H. It is worth mentioning that this step is critical since oxyhydroxides easily dissolve in acid. Higher concentrations and other acids, such as HCl, were also tested, resulting in the dissolution of the product.

Delamination and Restacking of γ-Nickel–Cobalt Oxyhydroxide Nanosheets in TBAOH

To maintain a 1:1 H^+:TBA^+ ratio, 0.5 g of NCOx-H was suspended in a mixture of H_2O:40% TBAOH (1.5M solution in water, obtained from Acros) containing 2.5 mL of TBAOH and 257.5 mL of H_2O. The solution was maintained under stirring for 90 days at room temperature. The resulting black suspension was then centrifuged at 5000 rpm for 10 min to remove impurities. Then, the supernatant solution was heated at 50 °C for 10 days to remove the solvent and induce restacking of the suspended nanoparticles. The final product (0.1 g) is designated as NCOx-TBA.

Physicochemical Characterization

Powder X-ray diffraction patterns were obtained using a PANalytical X'Pert Pro powder diffractometer in the Brag–Brentano geometry using a monochromator with $K\alpha_1$ line (λ = 1.5406 Å) at room temperature, with 2θ range from 8 to

80° with a 0.0170° measuring step. The material was previously ground to fine powder and measured on a steel powder specimen holder.

Scanning electron microscopy direct imaging was performed at the Plateform Aquitaine de Caractérisation des Matériaux (PLACAMAT) by means of a SEM-FEG HR (JEOL 6700F microscope). Transmission electron microscopy imaging was performed with a TEM JEOL JEM 1400 Plus microscope, while high-resolution imaging was obtained by means of a TEM-FEG HR (JEOL 2200FS microscope) working at 200 kV coupled to an EDX JEOL Si–Li detector with an image resolution of 0.19 nm and an EDS point resolution of 1.5 nm. The images for non-exfoliated samples were obtained by suspending a portion of the powder in ethanol and dropping it on top of a carbon-coated copper grid. In the case of exfoliated samples, an aliquot was taken of the exfoliated suspension and the carbon-coated grid was simply immersed in the solution.

Fourier transform infrared spectrometry was performed with Thermo Electron Corp. Nicolet 5700 equipment in specular mode for wave numbers from 400 to 4000 cm^{-1}. The powders were previously mixed with KBr at a 1:100 ratio and pressed into disks.

Raman measurements were performed by means of a Yvon Horiba LabRAM HR-800 microspectrometer with a 514.5 nm excitation wavelength (Ar^+ laser) and a power adjusted to ca. 50 µW to avoid any degradation of the sample or a LabRAM HR Evolution Raman spectrometer (HORIBA, Jobin Yvon, Edison, NJ, USA) with an operating laser at 532 nm.

Nitrogen adsorption/desorption isotherms were recorded using an ASAP 2020 (Micromeritics) at 377 K. Prior to the measurements, degasification at 80 °C for 300 min and at 110 °C for 200 min under high vacuum was performed. The Brunauer–Emmett–Teller specific surface area was computed using adsorption data in the relative pressure (P/P_o) range of 0.18–0.30. The pore size distribution was derived from the amounts adsorbed in the relative pressure range from 0.01 to 0.99 by means of the adsorption branch using the Barrett–Joyner–Halenda (BJH) method.

Elemental analysis (carbon, hydrogen, nitrogen, and sulfur content) was determined by combustion at 920 °C in a tin foil in excess of oxygen by means of a Thermo Flash EA 111E Series apparatus. Inductively coupled plasma–optical emission spectroscopy (ICP-OES) was used to obtain the concentrations of cobalt, nickel, sodium, and potassium. Results were obtained by dissolving 10–20 mg of the powder into HCl, diluted to a concentration in the 1–200 $mg{\cdot}L^{-1}$ range and analyzed by means of a Varian 720ES ICP-OES spectrometer.

The mean oxidation state of metal ions has been determined by iodometric titration. First, approximately 15 mg of the (hydr)oxide material was dissolved in 5 mL of H_2O, 10 mL of KI at 10 g/L, and, finally, 5 mL of HCl (37%). KI is added to reduce all of the transition metal ions that have an oxidation state superior to 2+, leading to the oxidation of I^- into I_2. Then, the solution is heated for total dissolution and I_2 is titrated with 0.1M $Na_2S_2O_3$. The mean oxidation state (x) is calculated using eq 1:

$$n_{I_2} = \frac{x-2}{2} n_{Me^{x+}} = \frac{1}{2}[S_2O_3^{2-}]V_{eq} \qquad (1)$$

where V_{eq} is the volume of sodium thiosulfate added at the equivalence. This procedure is repeated at least three times.

Atomic force microscopy (AFM) was used to measure the thickness of suspended delaminated nanoparticles. The aqueous suspension of tetrabutylammonium-intercalated nickel–cobalt oxyhydroxide was centrifuged at 14600 rpm for 10 min. The resulting supernatant solution was isolated and diluted to double their volume. A 1 mL aliquot of the diluted solution was drop-cast on top of a mica surface and dried at 40 °C for 7 days. A Nanosurf AFM in tapping mode with a silicon point–probe-plus Nanosensor cantilever (PPP-NCLAuD-10, gold coated with a resonance frequency of 315 kHz) was used to obtain the delaminated sample topography. The average nanoparticle thickness was determined from at least 4 regions in 2–4 μm^2 AFM images.

Electrochemical Characterization

The electrode material consisted of 80% active material, 15% active carbon, and 5% of PTFE (Sigma-Aldrich) as binder. The mass of the components was determined by means of a microbalance Sartorius MC5-0CE with an accuracy of 0.01 mg. Once the electrode material was formed, a round area of 1 cm^2 was pressed on a stainless-steel grid by applying 7 tons by means of a hydraulic cylinder press. The mass of active material varied between 1.5 mg and 9.5 mg.

All electrochemical measurements were performed with a three-electrode electrochemical cell by means of an Interface IFC1000-07087 potentiostat (Gamry Instruments). Platinum foil of 2.5 cm × 2.5 cm was used as counter electrode, while a SCE electrode was used as reference. 1M LiOH and 1M KOH were used as electrolytes.

Cyclic voltammetry was carried out at different scan rates (1–20 $mV{\cdot}s^{-1}$) in a potential window ranging from −0.5 V to 0.65 V (vs SCE) and an initial activation of 5–10 cycles. Galvanostatic charge–discharge was also carried out at different current densities (1–10 $A{\cdot}g^{-1}$) in a similar potential range. Lifetime cycling tests were performed during 5000 charge–discharge cycles at 10 $A{\cdot}g^{-1}$.

Results and Discussion

Physicochemical Characterization

The procedure used in the delamination of nickel–cobalt oxide nanosheets is exemplified in Figure 1. Essentially, α-Ni-Co(OH)$_2$·(CO_3^{2-},2NO_3^-)$_x$·(H_2O)$_y$ {NCOH} is synthesized by coprecipitation. This is followed by oxidation in NaClO/KOH into γ-(Ni–Co)O_2·(H^+,Na^+,K^+)$_x$·(H_2O)$_y$ {NCOx-HNK} and protonation into γ-(Ni–Co)O_2·(H^+)$_x$·(H_2O)$_y$ {H-NCOx-H}. Then, the powder is suspended in a TBA–OH solution, where it gets exfoliated in small nanoslabs of γ-(Ni–Co)O_2 that are suspended in solution. By means of solvent evaporation the material becomes restacked {NCOx-TBA}.

X-ray Diffraction

XRD results are presented in Figure 2. In accordance to literature, the patterns were indexed with a hexagonal cell. [25] Supporting Information Figure S1 presents X-ray diffraction patterns of nickel hydroxide and cobalt oxyhydroxide as reference. The diffraction peak at the lowest angle, indexed as (001) reflection, has its inter-reticular distance that corresponds to the interslab distance, i.e., the distance between two adjacent metal planes, while the (110) reflection corresponds to half of the metal–metal distance within the slab [25] and is therefore strongly influenced by the average metal oxidation state. In the pristine material, carbonate and nitrate anions are intercalated to maintain electroneutrality due to the excess charge introduced by Co(III), resulting in an interslab distance close to 7.93 Å, as reported by Delmas et al. [26] The metal–metal slab distance (a_{hex} parameter value) obtained for the α phase is 3.04 Å, in accordance with literature [25] and with the value expected for Ni^{2+} ions coexisting with a certain number of Co^{3+} ions.

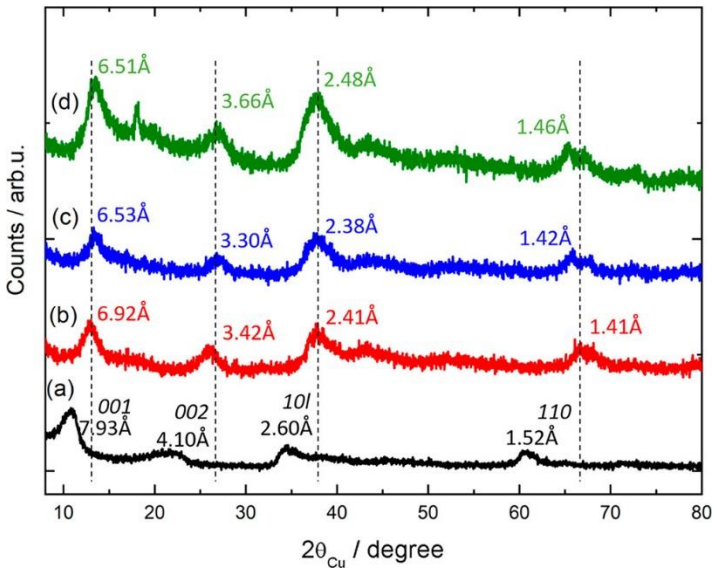

Figure 2. X-ray diffraction patterns for (a) NCOH used as reference, (b) NCOx-HNK, (c) NCOx-H, and (d) restacked NCOx-TBA. The numbers correspond to the inter-reticular distances calculated on the basis of indexation with a hexagonal cell.

After oxidation in NaClO/KOH (Figure 2b–d), the (110) reflection is shifted toward a higher angle and the inter-reticular distance obtained is close to 1.40 Å, which is consistent with the oxidation of nickel and cobalt ions to an average oxidation state of 3.2+, as confirmed by iodometric titration, presented in Table S1. The resulting material (Figure 2b) γ-(Ni–Co)O_2·(H^+,Na^+,K^+)$_x$(H_2O)$_y$, exhibits the (001) diffraction peak at 6.92 Å. This interslab distance decreases when compared to the pristine material, due to the modification of the interslab composition resulting from the decarbonization, which provokes the intercalation of alkali cations present in the medium (Na^+,K^+) to maintain electroneutrality.
The material is then acidified (Figure 2c) to substitute the alkali ions in the interslab space for protons, since H^+ ions have better affinity to TBA–OH ions and exfoliation can only be achieved with this intermediate step. [27] The substitution of alkali cations in the interslab space to the smaller protons shortens the interslab distance ((001) reflection) of NCOx-H to 6.53 Å. During the subsequent steps, TBA^+ intercalation and exfoliation, the (110) line is almost not shifted, which shows that the metal oxidation state reached is maintained. Finally, once the material is exfoliated and restacked by TBA^+ intercalation and solvent evaporation (Figure 2d), the material becomes restacked with an interslab distance of 6.51 Å, indicating that the nature of the material is preserved during the exfoliation process.

In summary, nickel–cobalt oxyhydroxide slabs (with oxidation state of 3.2+, as evidenced by iodometric titration) are separated by intercalated protons, potassium and sodium ions, and water molecules. During the acid treatment, sodium and potassium ions are substituted by protons. Considering their smaller size, the insterslab distance slightly decreases to 6.53 Å. Then, the material is introduced in a solution of TBA^+, for protons to be substituted by TBA^+, whose bigger molecular size increases the interslab distance to reach delamination. Considering that the delaminated material is in suspension, the material was precipitated by solvent evaporation. During solvent evaporation, the slabs restacked, preserving their nature and resulting in a material similar to the predelaminated precursor that has protons intercalated (widely available in the aqueous solvent), thus yielding a similar, yet slightly lower, interslab distance as the protonated material (6.51 Å). This process is depicted in Figure 1.

Elemental Analysis

The results of elemental chemical analysis, displayed in Table S2, indicate at first that cobalt and nickel are present in a 0.65/0.35 atomic ratio, which is maintained during the entire process, exemplifying that the reactions are topotactic and preserve slab integrity. Once the pristine hydroxide material (NCOH) is oxidized to oxyhydroxide (NCOx-HNK), significant amounts of potassium and sodium are present within the material, as expected from literature. [(26)] During protonation (NCOx-H), there is an overall decrease on the amount of intercalated cations. Nonetheless, their substitution for proton ions is not complete. Finally, after exfoliation and restacking in TBAOH, the carbon signal dramatically augments and nitrogen is still present, while the relative weight percentages of nickel and cobalt diminish, showing that TBA^+ ions are still within the material. Additional purification steps are therefore required to successfully remove TBA^+ since rinsing with ethanol, acetone, and water cannot completely remove the organic material.

Scanning and Transmission Electron Microscopy

The evolution of the material's morphology throughout the synthesis procedure is studied by means of SEM and TEM. The size of aggregates is reduced with each step of the synthesis. Initially, NCOH consists of big aggregates of densely packed particles (>10 µm) (Figure 3a). After oxidation, NCOx-NKH presents a very similar morphology (Figure 3b). However, the domain size of the particles is slightly reduced. Acidification further decreases the size of the aggregates to particles of 5 µm or smaller size, with a very heterogeneous distribution (Figure 3c). After TBAOH exfoliation and restacking by evaporation (Figure 3d), the particle size distribution becomes more homogeneous and particles decrease their domain size to approximately 1 µm diameter, although bigger particles can still be found. Thus, porosity and surface area seem to increase at every step of the exfoliation procedure.

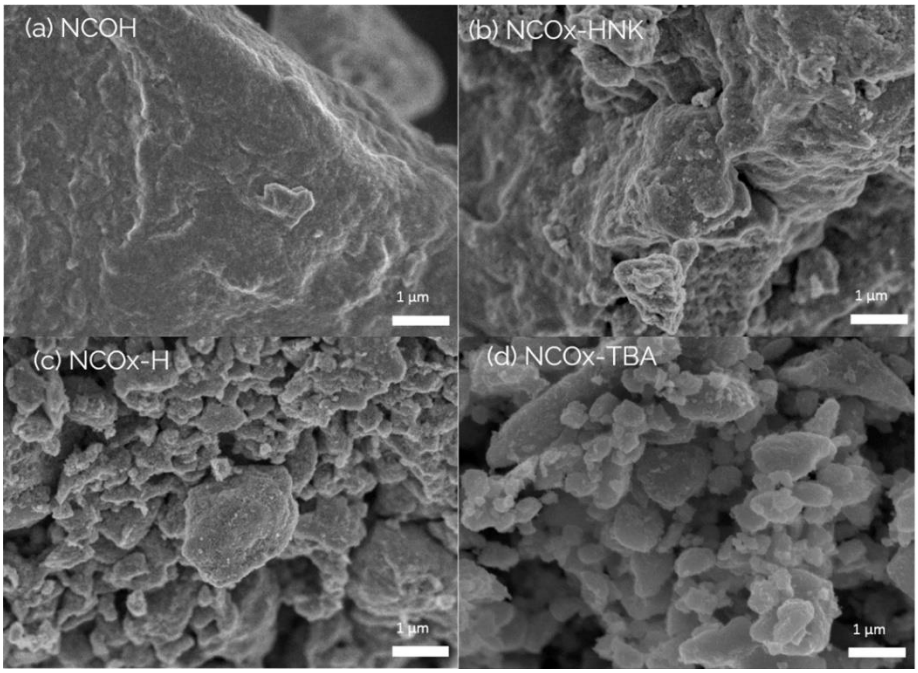

Figure 3. Scanning electron microscopy images of (a) NCOH, (b) NCOx-HNK, (c) NCOx-H, and (d) restacked NCOx-TBA after delamination in TBAOH and restacking by solvent evaporation.

TEM results, shown in Figure 4, provide additional morphological information. NCOx-HKN consists of big aggregates (>200 nm) that present randomly oriented nanostructured domains. Thus, nanoparticles of approximately 1–10 nm aggregate in random directions, resulting in the formation of secondary microparticles that should correspond to crystallites, considering the broad diffraction peaks observed in Figure 2. A similar structure can be observed once the material is acidified (Figure 4b). However, both the aggregates (>500 nm) and the coherent domains within the particles are bigger in this case, ranging from 15 to 25 nm size. Once exfoliated by TBA^+ intercalation, dispersed particles of 10–20 nm diameter size are obtained (Figure 4c). Given the thin nature of these nanoslabs, it is challenging to obtain TEM images with good resolution. However, it seems that the nanoslabs also consist of smaller coherent domains of 1–20 nm, maintaining the nature of the bulk material. It is worth mentioning that, in addition to these smaller sized particles, bigger aggregates can also be found, which shall be separated by centrifugation at higher speeds (>15000 rpm). Finally, once the material is restacked, a granulated morphology similar to the starting material is obtained (Figure 4d). Images of these materials at different magnifications can be found in the Supporting Information (Figure S2).

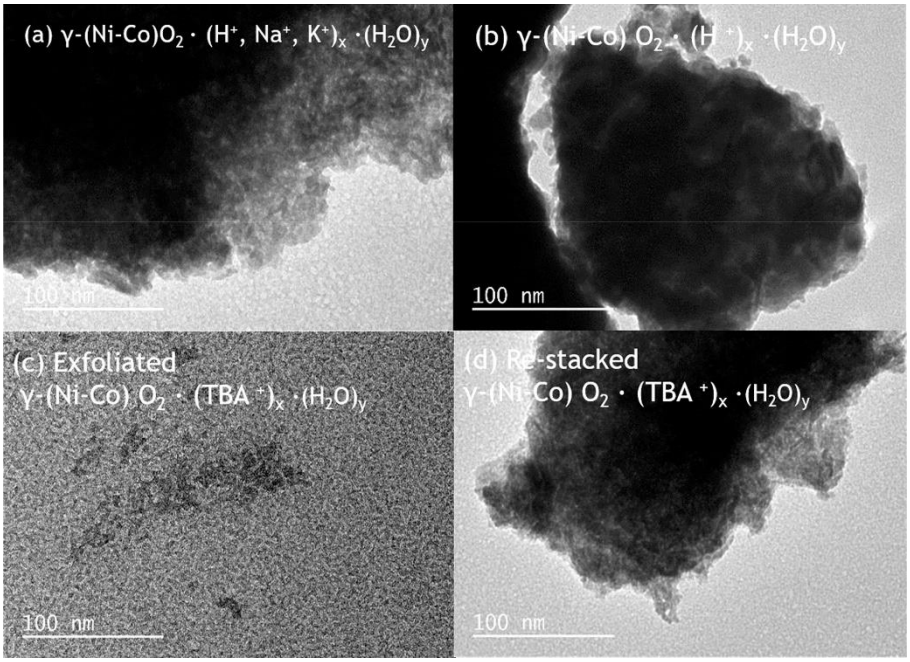

Figure 4. Transmission electron microscopy images of (a) NCOx-HNK and (b) NCOx-H, (c) exfoliated oxide slabs in TBAOH (NCOx-TBA), and (d) restacked NCOx-TBA.

Fourier Transform Infrared and Raman Spectroscopy

When FTIR results are considered, NCOH (Figure 5a) is characterized by a large broad signal at 3446 cm^{-1} and a large band and 1646 cm^{-1} (stretching and bending vibrations of water molecules), a strong narrow peak at 1376 cm^{-1} assigned to vibrations of monodentate carbonate and nitrate anions and, finally, a broad band centered at 673 cm^{-1} and a narrow peak at 522 cm^{-1} that corresponds to stretching vibrations of metal–oxygen bonds (M–O). When the material is oxidized (Figure 5b), the signals associated with vibration modes of water become mitigated, while the peaks associated with carbonate anions disappear. On the other hand, a double peak at 570 and 632 cm^{-1} appears that corresponds to M–OH and M-O stretching vibrations. When the sample is protonated (Figure 5c), this low-wavenumber peak becomes intensified, while signals associated with water molecules become weaker. Finally, after exfoliation and restacking (Figure 5d), FTIR spectrum presents many additional peaks that are associated with TBA^+ molecules since ethanol and acetone rinsing is not enough to eliminate them. There are two main relevant features: (i) the signal for the bands associated with water molecules is increased (more water molecules intercalated in the interslab space of the restacked material are in accordance with the increased interslab distance observed by XRD, although they could be brought by the residual TBA^+); (ii) M–O and M–OH vibrations, visible at 500–700 cm^{-1}, are maintained and become more significant than in the α phase, in which they are barely visible. [28–32] Details on the 400–1000 cm^{-1} ranges can be found in Figure S3.

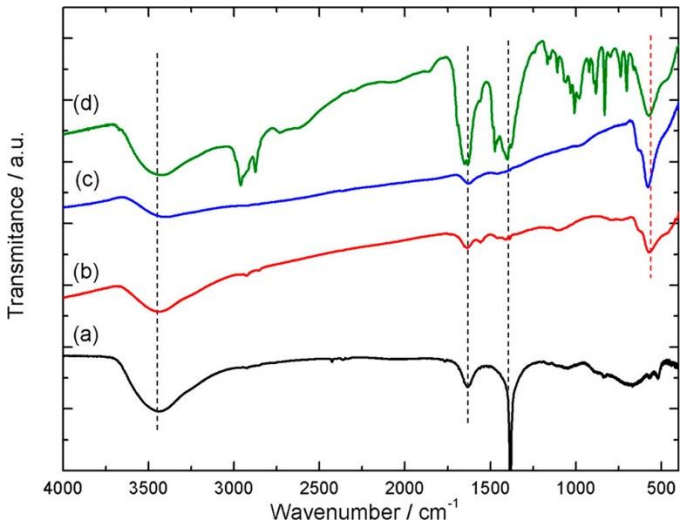

Figure 5. FTIR results for (a) NCOH, (b) NCOx-HNK, (c) NCOx-H, and (d) restacked NCOx-TBA.

Raman spectra, shown in Figure 6, provide additional evidence on the phase transformation processes during exfoliation. NCOH presents two main bands, at 464 and 528 cm^{-1}, assigned to M–OH and M–O vibration modes. When the material is oxidized, these two bands are present at approximately 451 and 527 cm^{-1} with different relative intensities, and a shoulder is observed around 580 cm^{-1}. This additional signal can also be detected in NCOx-HNK and may be associated with structural defects. Finally, a broad band from 400 to 700 cm^{-1} with 3–4 peaks is observed when the sample is exfoliated and restacked, corresponding to Co–O and Ni–O vibrations which might be influenced by the presence of TBA^+. However, this specific effect requires further study, which is out of the scope of the present work. [33,34]

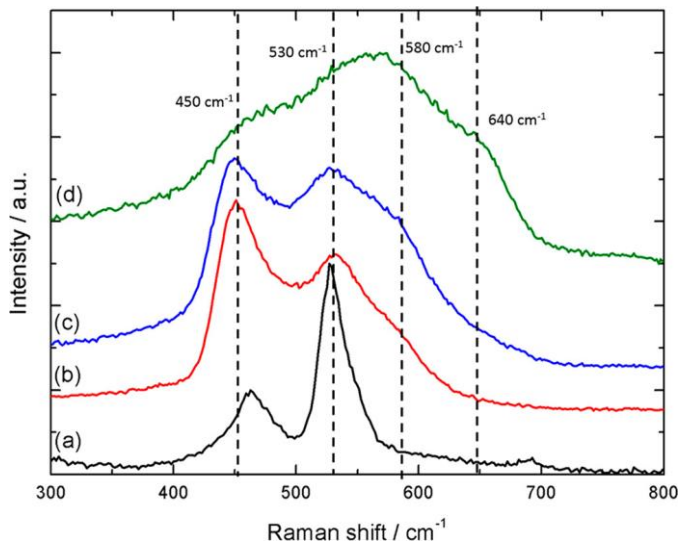

Figure 6. Raman results for (a) NCOH, (b) NCOx-HNK, (c) NCOx-H, and (d) restacked NCOx-TBA.

Nitrogen Adsorption Isotherms

The specific surface areas of NCOx-H and NCOx-TBA were analyzed by BET. Results, presented in Figures S4 and S5, show that both materials display a type IIB isotherm, characteristic of nonporous or macroporous materials, with a narrow hysteresis cycle, which indicates the presence of some mesopores. NCOx-H presents a specific surface area of 190 $m^2 \cdot g^{-1}$ with a relevant number of mesopores, while NCOx-TBA displays a specific surface area of only 94 $m^2 \cdot g^{-1}$. Results suggest that TBA^+ molecules intercalated in the interlayer space of the final material, as clearly observed by FTIR, reduce the N_2 adsorption surface area, which may result in a lower accessible active surface area and worsened electrode–electrolyte interaction in their evaluation as energy storage materials. In any case, a certain effect in the electrochemical behavior is expected from BET results.

Atomic Force Microscopy

AFM results for delaminated TBA^+-intercalated nickel–cobalt oxide in distilled water, diluted and drop-cast on top of mica, are presented in Figure 7. Results display a homogeneous dispersion of nanoparticles with different diameters, ranging from 30 to 175 nm. On the other hand, smaller particles present a thickness around 1.5–3 nm, while the biggest ones reach values up to 85.6 nm. Solvent molecules, aggregation during sample preparation for AFM measurements and trapped TBA^+ may increase the expected thickness of the nanolayers. Nonetheless, results present a great number of nanoparticles with a thickness of ~3 nm, associated with 2–3 monolayer stacks of nickel–cobalt oxyhydroxide, when compared to the theoretical value for a nickel–cobalt oxyhydroxide monolayer (0.52 nm) with adsorbed TBA^+ molecules, 0.84 nm in size, on its surface, as depicted in Figure 7. [35–37]

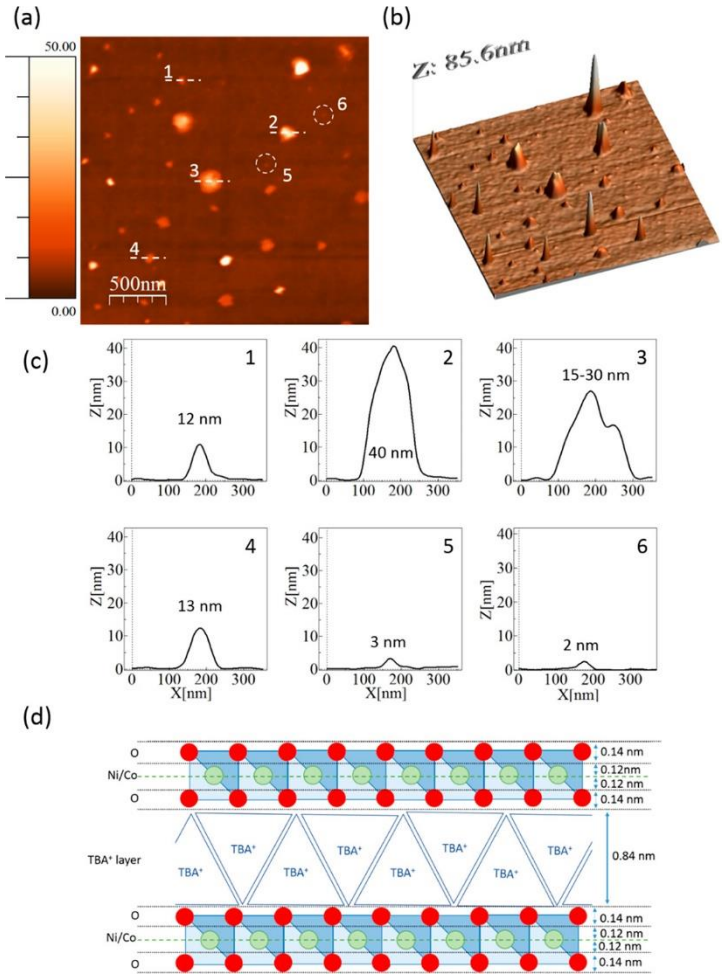

Figure 7. Atomic force microscopy topography (a) 2D image, (b) 3D image, and (c) height profiles of delaminated tetrabutylammonium-intercalated nickel–cobalt oxyhydroxide obtained in tapping-mode. Each dotted line corresponds to a height profile with the same numeration. (d) Schematic representation of theoretical values for a nickel–cobalt oxyhydroxide bilayer.

Electrochemical Characterization

This section aims at comparing the electrochemical behavior of nickel–cobalt oxyhydroxide during its delamination process to determine the effect of the intercalated species on their performances.

Study in 1M KOH Electrolyte

Cyclic voltammetry curves at 5 $mV \cdot s^{-1}$ are shown in Figure 8a in the potential range from −0.3 to 0.55 V (vs SCE). For the three materials, one anodic peak and its cathodic counterpart are observed, centered at approximately 0.3 V and −0.05 V

respectively, as expected for mixed nickel–cobalt hydroxides being reversibly oxidized to oxyhydroxides. [38,39] Galvanostatic discharge curves, Figure 8b, are characteristic of "battery" materials with faradaic processes. The best capacity results are obtained for the material after exfoliation–restacking (118.7 mA·h·g^{-1} at 1 A·g^{-1}) against 106.1 mA·h·g^{-1} and 76.8 mA·h·g^{-1} respectively for NCOx-HNK and protonated NCOx-H oxyhydroxides before exfoliation. It is worth mentioning that all of the materials exhibit high Coulombic efficiency, with 96%, 94%, and 98% for NCOx-HNK, NCOx-H, and NCOx-TBA, respectively, revealing their high energy efficiency. These results are likely caused by a better surface accessibility and electrode–electrolyte interaction by the delaminated material.

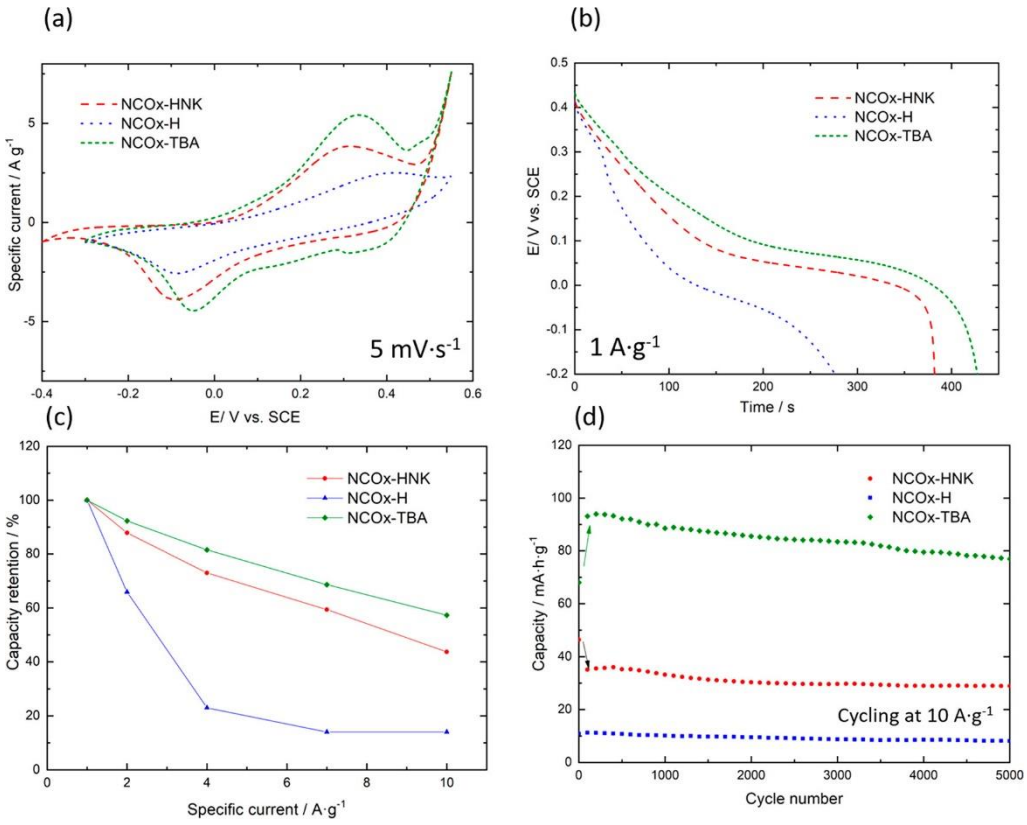

Figure 8. Comparison of the electrochemical response by (a) cyclic voltammetry, (b) galvanostatic discharge, (c) capacity retention at different applied current densities, and (d) capacity retention evaluated by galvanostatic continuous charge–discharge cycling during 5000 cycles at 10 A·g^{-1} for the different composites obtained during delamination of nickel–cobalt oxyhydroxide by TBA$^+$ intercalation in 1 M KOH.

The cycling behavior of the materials is presented in Figure 8d, with a detailed view of the first 200 cycles presented in Supporting Information Figure S6. The capacity for NCOx-HNK oxyhydroxide is reduced during the first 20 cycles and maintained henceforth. On the other hand, during the first 100 cycles, NCOx-TBA shows a strong increase in capacity. This evolution may be explained by the fact that, initially, the interference of TBA$^+$ impedes an optimal electrode–electrolyte interaction. After activation, TBA$^+$ is removed from the surface of the active material and there is an increase of the number of electrochemically active sites. However, defining the exact mechanism that induces an activation and increase in capacity for the delaminated material requires further investigation. Moreover, once activated, the capacity decay of this material is similar to the performance displayed by the parent oxyhydroxide materials. It is also worth considering the possible influence of TBA$^+$ ions to nickel–cobalt nanoslabs affecting the degradation of the material. After 5000 cycles, the capacity retention of the different materials is 62%, 74%, and 113% for NCOx-HNK, NCOx-H, and NCOx-TBA, respectively.

Finally, when higher current densities are applied (Figure 8c), the best rate capability is displayed by the exfoliated NCOx-TBA that retains up to a 57% of capacity, while a less promising performance is displayed for NCOx-HNK and NCOx-H with only 43% and 14% capacity retention, respectively, at the same applied current density. These results are likely caused by a better surface accessibility and electrode–electrolyte interaction by the delaminated material. Results concerning galvanostatic discharges at different applied current densities and cyclic voltammetries at different scan rates are displayed in detail in Figure S7.

Study in 1M LiOH Electrolyte

The electrochemical performance of the materials shown in Figure 9 has also been evaluated in 1M LiOH. The performances of NCOx-HNK and NCOx-H are slightly influenced by the change of electrolyte, with similar cycling performance and capacity values. Values of 112.6 and 91.0 $mA{\cdot}h{\cdot}g^{-1}$ are obtained at 1 $A{\cdot}g^{-1}$ for NCOx-HNK and NCOx-H, respectively, with a capacity retention of 63% and 67% after 5000 cycles in 1M LiOH. The main difference resides on the capacity retention obtained at higher applied current densities as displayed in Figure 9c.

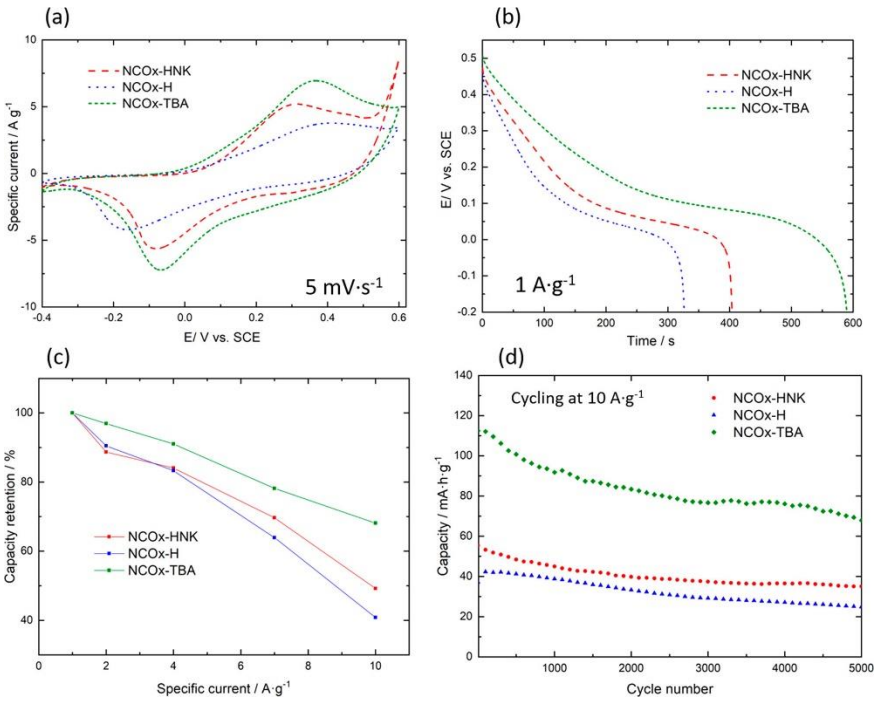

Figure 9. Comparison of the electrochemical response by (a) cyclic voltammetry, (b) galvanostatic discharge, (c) capacity retention at different applied current densities, and (d) capacity retention evaluated by galvanostatic continuous charge–discharge cycling during 5000 cycles at 10 $A{\cdot}g^{-1}$ for the different composites obtained during delamination of nickel–cobalt oxyhydroxide by TBA^+ intercalation in 1M LiOH.

There is an evident enhancement in performance for the restacked TBA^+-intercalated nickel–cobalt oxyhydroxide in LiOH compared to KOH, resulting in capacity values of 165.1 $mA{\cdot}h{\cdot}g^{-1}$ at 1 $A{\cdot}g^{-1}$ and 112.5 $mA{\cdot}h{\cdot}g^{-1}$ at 10 $A{\cdot}g^{-1}$. Moreover, the preactivation step required for NCOx-TBA in KOH reduces in LiOH at the first 10 cycles, as observed in Figure S8. A capacity retention of 60% for NCOx-TBA is obtained after 5000 cycles at 10 $A{\cdot}g^{-1}$. The Coulombic efficiency is similar to the results obtained in KOH electrolyte, although overall higher current efficiencies for the oxidized materials are obtained, with 97%, 98%, and 98% for NCOx-HNK, NCOx-H, and NCOx-TBA, respectively. In this case, the capacity of the exfoliated and restacked material is nearly 1.5 times the initial capacity displayed by the non-exfoliated oxyhydroxide at 1 $A{\cdot}g^{-1}$. Details on the performance of the different materials at different scan rates and applied current densities are provided in Figure S9.

On the one hand, whether in KOH or in LiOH, the significant increase in capacity between the exfoliated material and the parent oxyhydroxide may be explained by the increased electrode–electrolyte interaction and ease for electrolyte penetration within the material once it is exfoliated and restacked. Although BET indicates a more reduced surface area for NCOx-TBA, this may not correspond to the real electrochemically active surface of the material. TBA^+ initially blocks the access to the electrolyte and reduces the surface area. However, when immersed in electrolyte and after a certain activation process, TBA^+ is removed from the surface and a more intimate contact between active material and electrolyte can be achieved, increasing the number of active sites. Moreover, it is observed by TEM and SEM an apparent decrease on the microcrystalline structure (Figures 3 and 4). Possibly, when the material is exfoliated and restacked, the interaction between the nanoslabs is reduced, promoting electrolyte penetration and consequently an enhanced capacity response. Therefore, two factors can be considered as main contributors for the capacity increase of the material: reduction of the microcrystalline domain and weakened interslab interaction that promotes electrolyte penetration.

Moreover, the use of LiOH, as compared to KOH, may result in better faradaic charge-transfer phenomenon and better alkali ion penetration. As reported in literature, [(40)] LiOH is likely to inhibit oxygen evolution and therefore to favor material

oxidation. This is evident when cycling stability is evaluated in LiOH, since the material displays a more stable electrochemical response, with higher capacity that only requires 10 cycles to activate, in contrast to the activation observed when KOH is used.

In conclusion, the exfoliation of nickel–cobalt oxyhydroxide by means of TBA^+ intercalation proves that delamination is a successful route for the enhancement of the electrochemical properties of the material and that TBA^+ intercalation does not hamper the electrochemical response of the active material. Despite the preactivation step, especially required in 1M KOH, an optimized performance is observed in which an intimate active material–electrolyte contact is achieved. Thus, exfoliation routes of layered materials to obtain few-layer nanostructures have a positive impact on the electrochemical properties of the electrode material. A comparison with similar Ni–Co composite electrode materials from literature also validates the efficiency of the exfoliation–restacking approach, leading to materials that possess among the highest specific capacities (see Table 1).

Table 1. Comparison of the Electrode Material Performance with Other Electrode Materials Reported for Electrochemical Energy Storage Applications

material	synthesis	electrolyte	capacity	ref
NiCo–OH	refluxed at 90 °C	KOH	129 $mA{\cdot}h{\cdot}g^{-1}$ at 1 $A{\cdot}g^{-1}$	41
composite Ni–Co–Mn	electrochemical deposition	KOH	38 $mA{\cdot}h{\cdot}g^{-1}$ at 3 $A{\cdot}g^{-1}$	42
NiCo–LDH	hydrothermal method	KOH	121 $mA{\cdot}h{\cdot}g^{-1}$ at 0.5 $A{\cdot}g^{-1}$	43
Ni50Co50–LDH	refluxed at 90 °C	KOH	234 $mA{\cdot}h{\cdot}g^{-1}$ at 0.5 $A{\cdot}g^{-1}$	44
Ni–Co oxide	low temperature solution method	KOH	67 $mA{\cdot}h{\cdot}g^{-1}$ at 1 $A{\cdot}g^{-1}$	45
Ni–Co oxide	electrodeposition	KOH	113.4 $mA{\cdot}h{\cdot}g^{-1}$ at 1 $A{\cdot}g^{-1}$	46
NCOx–TBA	exfoliation restacking	LiOH KOH	165 $mA{\cdot}h{\cdot}g^{-1}$ at 1 $A{\cdot}g^{-1}$;118 $mA{\cdot}h{\cdot}g^{-1}$ at 1 $A{\cdot}g^{-1}$	this work

In principle, obtaining few-layer nanosheets of a lamellar material by delamination has two expected effects in the electrochemical performance. On the one hand, it serves as a precursor route to create composite materials that interact at an atomic level, combining the benefits of different materials. On the other hand, when a delaminated material is restacked, as in this case, there is an enhanced electrode–electrolyte interaction that leads to a better electrochemical performance. The results here [47] presented for the first time exemplify the potential application of delamination of layered materials for the synthesis of Ni–Co–Mn composites as an example.

Conclusions

Delamination of nickel–cobalt oxyhydroxide by intercalation of tetrabutylammonium in its interslab space has been proved as a successful route to enhance the electrochemical performance of nickel–cobalt oxyhydroxide by increasing the electrochemical active surface area and electrode–electrolyte interaction after an electrochemical activation process to remove residual TBA^+ cations. Results show a rise in capacity from 112 $mA{\cdot}h{\cdot}g^{-1}$ in 1M LiOH at 1 $A{\cdot}g^{-1}$ for the nondelaminated precursor to 165 $mA{\cdot}h{\cdot}g^{-1}$ after exfoliation and restacking, phenomena associated with better electrode–electrolyte interaction. Moreover, the influence of the electrolyte cation has been studied, resulting in a shorter activation period for lithium than for potassium hydroxide, which has been associated with better alkali ion penetration, as a consequence of lower ion hydration sphere. Overall, results are greatly dependent on the intercalated ions in the interslab, which is directly correlated to the electrochemical performance of the material.

Supporting Information

The Supporting Information is available free of charge at https://pubs.acs.org/doi/10.1021/acsaem.2c01905.

XRD diffraction patterns, iodometric titrations, chemical analyses, TEM images, FTIR results, BET isotherms, 200 initial cycles continuous charge–discharge comparison, cyclic voltammetries, and galvanostatic charge–discharge curves (PDF)

Author Information

- Corresponding Author : Liliane Guerlou-Demourgues - Bordeaux INP, ICMCB UMR 5026, CNRS, University of Bordeaux, 33600Pessac, France; RS2E, Réseau Français sur le Stockage Electrochimique de l'Energie, CNRS 345980039Amiens Cedex 1, France; Email: Liliane.Guerlou-Demourgues@enscbp.fr
- Authors : Alberto Adan-Mas - Centro de Química Estrutural-CQE, DEQ, Instituto Superior Técnico, Universidade de Lisboa, 1049-001Lisboa, Portugal; Bordeaux INP, ICMCB UMR 5026, CNRS, University of Bordeaux, 33600Pessac,

France; https://orcid.org/0000-0003-0790-3467

Jacob Olchowka - Bordeaux INP, ICMCB UMR 5026, CNRS, University of Bordeaux, 33600Pessac, France; RS2E, Réseau Français sur le Stockage Electrochimique de l'Energie, CNRS 345980039Amiens Cedex 1, France; https://orcid.org/0000-0001-7430-0266

Lydie Bourgeois - Groupe de Spectroscopie Moléculaire, Université de Bordeaux, ISM, F-33405Talence, France; Bordeaux INP, ISM, CNRS UMR 5255, F-33405Talence, France

Philippe Legros - PLACAMAT UMS 3626, CNRS-Université de Bordeaux, F-33608Pessac Cédex, France

Patrizia Paradiso - IDMEC–Instituto de Engenharia Mecánica, Universidade de Lisboa, 1049-001Lisboa, Portugal

Fátima Montemor - Centro de Química Estrutural-CQE, DEQ, Instituto Superior Técnico, Universidade de Lisboa, 1049-001Lisboa, Portugal

- Author Contributions : The manuscript was written through contributions of all authors. All authors have given approval to the final version of the manuscript. A.A.-M., J.O., and L.G.-D. participated in the conceptualization, data acquisition, curation and analysis, validation of results, and writing. F.M. contributed to the conceptualization, data analysis, methodology, review, and editing. L.B., P.L., and P.P. contributed with acquisition and analysis of data, methodology, review, and editing.

- Notes **:** The authors declare no competing financial interest.

Acknowledgments
This work is dedicated to the memory of Patrizia Paradiso. This work has been performed in the scope of the International Doctoral Program in Functional Materials (IDS-FunMat, Erasmus Mundus) and funded by the European Union. We express our gratitude to the Fundação para a Ciência e Tecnologia (FCT) for the funding under Contracts M-ERA.NET/0004/2014, PTDC/QUI-ELT/28299/2017, and UID/QUI/00100/2019. We also acknowledge Laura Ilharco for her assistance in BET measurements and interpretation, Auguste Fernandes in his aid for FTIR spectra acquisition, Kush Kumar Upadhyay for electrochemical discussion, Laetitia Etienne for CHNS and ICP measurements, Eric Lebraud for performing the XRD experiments, Catherine Denage, Sabine Goma, and Philippe Dagault for their general assistance, and Marion Gayot and Sonia Buffière for assisting with TEM analysis at PLACAMAT (Plateforme Aquitaine de Caractérisation des Matériaux UMS 3626 CNRS-Université de Bordeaux, Pessac, France).

References

1 Pomerantseva, E.; Bonaccorso, F.; Feng, X.; Cui, Y.; Gogotsi, Y. Energy Storage: The Future Enabled by Nanomaterials. *Science* **2019**, *366* (6468), eaan8285, DOI: 10.1126/science.aan8285

2 Wang, Q.; O'Hare, D. Recent Advances in the Synthesis and Application of Layered Double Hydroxide (LDH) Nanosheets. *Chem. Rev.* **2012**, *112*, 4124– 4155, DOI: 10.1021/cr200434v

3 Adachi-Pagano, M.; Forano, C.; Besse, J.-P. Delamination of Layered Double Hydroxides by Use of Surfactants. *Chem. Commun.* **2000**, 91– 92, DOI: 10.1039/a908251d

4 O'Leary, S.; O'Hare, D.; Seeley, G. Delamination of Layered Double Hydroxides in Polar Monomers : New LDH-Acrylate Nanocomposites †. *Chem. Commun.* **2002**, 1506– 1507, DOI: 10.1039/b204213dISTEX

5 Jobbágy, M.; Regazzoni, A. E. Delamination and Restacking of Hybrid Layered Double Hydroxides Assessed by in Situ XRD. *J. Colloid Interface Sci.* **2004**, *275*, 345– 348, DOI: 10.1016/j.jcis.2004.01.082ISTEX

6 Hibino, T.; Jones, W. New Approach to the Delamination of Layered Double Hydroxides. *J. Mater. Chem.* **2001**, *11*, 1321–1323, DOI: 10.1039/b101135iISTEX

7 Ma, R.; Liu, Z.; Takada, K.; Iyi, N.; Bando, Y.; Sasaki, T. Synthesis and Exfoliation of Co2+-Fe3+ Layered Double Hydroxides: An Innovative Topochemical Approach. *J. Am. Chem. Soc.* **2007**, *129*, 5257– 5263, DOI: 10.1021/ja0693035ISTEX

8 Hibino, T.; Kobayashi, M. Delamination of Layered Double Hydroxides in Water. *J. Mater. Chem.* **2005**, *15*, 653– 656, DOI: 10.1039/b416913aISTEX

9 Jaubertie, C.; Holgado, M. J.; San Roman, M. S.; Rives, V. Structural Characterization and Delamination of Lactate-Intercalated Zn, Al-Layered Double Hydroxides. *Chem. Mater.* **2006**, *18* (13), 3114– 3121, DOI: 10.1021/cm060512yISTEX

10 Ida, S.; Shiga, D.; Koinuma, M.; Matsumoto, Y. Synthesis of Hexagonal Nickel Hydroxide Nanosheets by Exfoliation of Layered Nickel Hydroxide Intercalated with Dodecyl Sulfate Ions. *J. Am. Chem. Soc.* **2008**, *130* (43), 14038– 14039, DOI: 10.1021/ja804397nISTEX

11 Vadivel, S.; Srimanon, K.; Sawangphruk, M. Regulating the Cationic Rearrangement of Ni-Rich Layered Oxide Cathode for High-Performance Li-Ion Batteries. *J. Power Sources* **2022**, *537*, 231526, DOI: 10.1016/j.jpowsour.2022.231526

12 Chen, Y.; Yang, J.; Yu, H.; Zeng, J.; Li, G.; Chang, B.; Wu, C.; Guo, X.; Chen, G.; Zheng, L.; Wang, X. Design and Preparation of NiCoMn Ternary Layered Double Hydroxides with a Hollow Dodecahedral Structure for High-Performance Asymmetric Supercapacitors. *ACS Appl. Energy Mater.* **2022**, *5* (6), 6772– 6782, DOI: 10.1021/acsaem.2c00385

13 Wang, G.; Zhang, L.; Zhang, J. A Review of Electrode Materials for Electrochemical Supercapacitors. *Chem. Soc. Rev.* **2012**, *41*, 797, DOI: 10.1039/C1CS15060J

14 Olchowka, J.; Tailliez, T.; Bourgeois, L.; Dourges, M. A.; Guerlou-Demourgues, L. Ionic Liquids to Monitor the Nano-Structuration and the Surface Functionalization of Material Electrodes: A Proof of Concept Applied to Cobalt Oxyhydroxide. *Nanoscale Adv.* **2019**, *1* (6), 2240– 2249, DOI: 10.1039/C9NA00171A

15 Invernizzi, R.; Guerlou-Demourgues, L.; Weill, F.; Lemoine, A.; Dourges, M. A.; Baraille, I.; Flahaut, D.; Olchowka, J. Controlled Nanostructuration of Cobalt Oxyhydroxide Electrode Material for Hybrid Supercapacitors. *Materials* **2021**, *14* (9), 2325, DOI: 10.3390/ma14092325

16 Schneiderová, B.; Demel, J.; Pleštil, J.; Janda, P.; Bohuslav, J.; Ihiawakrim, D.; Ersen, O.; Rogez, G.; Lang, K. Nickel Hydroxide Ultrathin Nanosheets as Building Blocks for Electrochemically Active Layers. *J. Mater. Chem. A Mater.* **2013**, *1* (37), 11429, DOI: 10.1039/c3ta12129a

17 Schneiderová, B.; Demel, J.; Pleštil, J.; Tarábková, H.; Bohuslav, J.; Lang, K. Electrochemical Performance of Cobalt Hydroxide Nanosheets Formed by the Delamination of Layered Cobalt Hydroxide in Water. *Dalton Trans.* **2014**, *43* (27), 10484, DOI: 10.1039/c4dt00141a

18 Schneiderová, B.; Demel, J.; Zhigunov, A.; Bohuslav, J.; Tarábková, H.; Janda, P.; Lang, K. Nickel-Cobalt Hydroxide Nanosheets : Synthesis, Morphology and Electrochemical Properties. *J. Colloid Interface Sci.* **2017**, *499*, 138– 144, DOI: 10.1016/j.jcis.2017.03.096

19 Liu, Z. H.; Ooi, K.; Kanoh, H.; Tang, W. P.; Tomida, T. Swelling and Delamination Behaviors of Birnessite-Type Manganese Oxide by Intercalation of Tetraalkylammonium Ions. *Langmuir* **2000**, *16* (9), 4154– 4164, DOI: 10.1021/la9913755ISTEX

20 Ma, R.; Sasaki, T. Nanosheets of Oxides and Hydroxides: Ultimate 2D Charge-Bearing Functional Crystallites. *Adv. Mater.* **2010**, *22* (45), 5082– 5104, DOI: 10.1002/adma.201001722ISTEX

21 Tang, C.; Giaume, D.; Guerlou-demourgues, L.; Lefèvre, G.; Barboux, P. Prediction of Isoelectric Point of Manganese and Cobalt Lamellar Oxides : Application to Controlled Synthesis of Mixed Oxides. *Langmuir* **2018**, *34* (23), 6670– 6677, DOI: 10.1021/acs.langmuir.8b00190

22 Tang, C.; Giaume, D.; Weill, F.; Penin, N.; Dourges, M. A.; Saadaoui, H.; Guerlou-Demourgues, L. Synergy of Mn and Co in Slab-Based Nanocomposites for Hybrid Supercapacitors: Impact of Restacking Process on Electrochemical Properties. *ACS Appl. Energy Mater.* **2019**, *2* (11), 7832– 7842, DOI: 10.1021/acsaem.9b01263

23 Fukuda, K.; Nakai, I.; Ebina, Y.; Ma, R.; Sasaki, T. Colloidal Unilamellar Layers of Tantalum Oxide with Open Channels. *Inorg. Chem.* **2007**, *46* (12), 4787– 4789, DOI: 10.1021/ic7004002ISTEX

24 Kim, T. W.; Oh, E.-J.; Jee, A.-Y.; Lim, S. T.; Park, D. H.; Lee, M.; Hyun, S.-H.; Choy, J.-H.; Hwang, S.-J. Soft-Chemical Exfoliation Route to Layered Cobalt Oxide Monolayers and Its Application for Film Deposition and Nanoparticle Synthesis. *Chem.–Eur. J.* **2009**, *15* (41), 10752– 10761, DOI: 10.1002/chem.200901590ISTEX

25 Faure, C.; Delmas, C.; Fouassier, M. Characterization of a Turbostratic α-Nickel Hydroxide Quantitatively Obtained from an NiSO4 Solution. *J. Power Sources* **1991**, *35*, 279– 290, DOI: 10.1016/0378-7753(91)80112-BISTEX

26 Faure, C.; Delmas, C.; Willmann, P. Preparation and Characterization of Cobalt-Substituted α-Nickel Hydroxide Stable in KOH Medium Part II. α-Hydroxide with a Turbostratic Structure. *J. Power Sources* **1991**, *35* (3), 263– 277, DOI: 10.1016/0378-7753(91)80111-AISTEX

27 Gao, Q.; Giraldo, O.; Tong, W.; Suib, S. L. Preparation of Nanometer-Sized Manganese Oxides by Intercalation of Organic Ammonium Ions in Synthetic Birnessite OL-1. *Chem. Mater.* **2001**, *13* (3), 778– 786, DOI: 10.1021/cm000426cISTEX

28 Xu, Z. P.; Zeng, H. C. Interconversion of Brucite-like and Hydrotalcite-like Phases in Cobalt Hydroxide Compounds. *Chem. Mater.* **1999**, *11* (1), 67– 74, DOI: 10.1021/cm980420bISTEX

29 Hu, Z.-A.; Xie, Y.-L.; Wang, Y.-X.; Xie, L.-J.; Fu, G.-R.; Jin, X.-Q.; Zhang, Z.-Y.; Yang, Y.-Y.; Wu, H.-Y. Synthesis of α-Cobalt Hydroxides with Different Intercalated Anions and Effects of Intercalated Anions. *J. Phys. Chem. C* **2009**, *113*, 12502– 12508, DOI: 10.1021/jp8106809

30 Yuan, H.; Dubbink, D.; Besselink, R.; Ten Elshof, J. E. The Rapid Exfoliation and Subsequent Restacking of Layered Titanates Driven by an Acid-Base Reaction. *Angew. Chem., Int. Ed.* **2015**, *54* (32), 9239– 9243, DOI: 10.1002/anie.201502539ISTEX

31 Ishijima, Y.; Okaniwa, M.; Oaki, Y.; Imai, H. Two Exfoliation Approaches for Organic Layered Compounds: Hydrophilic and Hydrophobic Polydiacetylene Nanosheets. *Chem. Sci.* **2017**, *8* (1), 647– 653, DOI: 10.1039/C6SC03350D

32 Faure, C.; Delmas, C.; Fouassier, M.; Willmann, P. Preparation and Characterization of Cobalt-Substituted α-Nickel Hydroxides Stable in KOH Medium Part I. A'-Hydroxide with an Ordered Packing. *J. Power Sources* **1991**, *35* (3), 249– 261, DOI: 10.1016/0378-7753(91)80110-JISTEX

33 Zhong, J.-H.; Wang, A.-L.; Li, G.-R.; Wang, J.-W.; Ou, Y.-N.; Tong, Y.-X. Co3O4/Ni(OH)2 Composite Mesoporous Nanosheet Networks as a Promising Electrode for Supercapacitor Applications. *J. Mater. Chem.* **2012**, *22* (12), 5656, DOI: 10.1039/c2jm15863a

34 Diaz-Morales, O.; Ferrus-Suspedra, D.; Koper, M. T. M. The Importance of Nickel Oxyhydroxide Deprotonation on Its Activity towards Electrochemical Water Oxidation. *Chem. Sci.* **2016**, *7* (4), 2639– 2645, DOI: 10.1039/C5SC04486C

35 Omomo, Y.; Sasaki, T.; Wang, L.; Watanabe, M. Redoxable Nanosheet Crystallites of MnO2 Derived via Delamination of a Layered Manganese Oxide. *J. Am. Chem. Soc.* **2003**, *125* (12), 3568– 3575, DOI: 10.1021/ja021364pISTEX

36 Oliva, P.; Leonardi, J.; Laurent, J. F.; Delmas, C.; Braconnier, J. J.; Figlarz, M.; Fievet, F.; Guibert, A. de. Review of the Structure and the Electrochemistry of Nickel Hydroxides and Oxy-Hydroxides. *J. Power Sources* **1982**, *8* (2), 229– 255, DOI: 10.1016/0378-7753(82)80057-8ISTEX

37 Tang, C. Exfoliation and Restacking of Manganese and Cobalt Based Lamellar Oxides for Supercapacitor Electrodes. Ph.D. Thesis, Université de Bordeaux, Bordeaux, France, 2017. https://tel.archives-ouvertes.fr/tel-01696266

38 Delmas, C.; Faure, C.; Borthomieu, Y. The Effect of Cobalt on the Chemical and Electrochemical Behaviour of the Nickel Hydroxide Electrode. *Mater. Sci. Eng., B* **1992**, *13* (2), 89– 96, DOI: 10.1016/0921-5107(92)90147-2ISTEX

39 Wang, L.; Zhang, L.; Ma, W.; Wan, H.; Zhang, X.; Zhang, X.; Jiang, S.; Zheng, J. Y.; Zhou, Z. In Situ Anchoring Massive Isolated Pt Atoms at Cationic Vacancies of α-NixFe1-x(OH)2 to Regulate the Electronic Structure for Overall Water Splitting. *Adv. Funct Mater.* **2022**, *32* (31), 2203342, DOI: 10.1002/adfm.202203342

40 Delmas, C; Borthomieu, Y; FAURE, C; Delahaye, A; Figlarz, M Nickel Hydroxide and Derived Phases Obtained by Chimie Douce from NaNiO2. *Solid State Ion* **1989**, *32-33*, 104– 111, DOI: 10.1016/0167-2738(89)90209-9ISTEX

41 Yang, J.; Yu, C.; Hu, C.; Wang, M.; Li, S.; Huang, H.; Bustillo, K.; Han, X.; Zhao, C.; Guo, W.; Zeng, Z.; Zheng, H.; Qiu, J. Surface-Confined Fabrication of Ultrathin Nickel Cobalt-Layered Double Hydroxide Nanosheets for High-Performance Supercapacitors. *Adv. Funct Mater.* **2018**, *28* (44), 1803272, DOI: 10.1002/adfm.201803272

42 Reghu Nath, A.; Jayachandran, A.; Sandhyarani, N. Nanosheets of Nickel, Cobalt and Manganese Triple Hydroxides/Oxyhydroxides as Efficient Electrode Materials for Asymmetrical Supercapacitors. *Dalton Trans.* **2019**, *48* (13), 4211– 4217, DOI: 10.1039/C9DT00302A

43 Lan, Y.; Li, M.; Fan, W.; Deng, Q.; Zeng, Z.; Wang, J.; Deng, S. Functional Molecules Regulated and Intercalated Nickel-Cobalt LDH Nano-Sheets on Carbon Fiber Cloths as an Advanced Free-Standing Electrode for High-Performance Asymmetric Supercapacitors. *Electrochim. Acta* **2019**, *321*, 134708, DOI: 10.1016/j.electacta.2019.134708

44 Li, R.; Hu, Z.; Shao, X.; Cheng, P.; Li, S.; Yu, W.; Lin, W.; Yuan, D. Large Scale Synthesis of NiCo Layered Double Hydroxides for Superior Asymmetric Electrochemical Capacitor. *Sci. Rep* **2016**, *6*, 18737, DOI: 10.1038/srep18737

45 Kim, D. K.; Hwang, M.; Ko, D.; Kang, J.; Seong, K.; Piao, Y. Electrochemical Performance of 3D Porous Ni-Co Oxide with Electrochemically Exfoliated Graphene for Asymmetric Supercapacitor Applications. *Electrochim. Acta* **2017**, *246*, 680– 688, DOI: 10.1016/j.electacta.2017.06.099

46 Adán-Más, A.; Silva, T. M.; Guerlou-Demourgues, L.; Bourgeois, L.; Labrugere-Sarroste, C.; Montemor, M. F. Nickel-Cobalt Oxide Modified with Reduced Graphene Oxide: Performance and Degradation for Energy Storage Applications. *J. Power Sources* **2019**, *419*, 12– 26, DOI: 10.1016/j.jpowsour.2019.02.055

47 Adán-Más, A. *Advanced metal graphene composite electrodes for a new generation of electrochemical energy storage devices*. Doctoral dissertation, Université de Bordeaux and Instituto Superior Técnico de Universidade de Lisboa, Bordeaux, France and Lisboa, Portugal, 2018. https://tel.archives-ouvertes.fr/tel-02054678v2